Radiological Technology (13:30 ～16:10 Lecture Room 2)

Session chairs: Prof. Yoshie Kodera
Associate Prof. Masatoshi Tsuzaka

ADVANCEMENT OF MEDICAL IMAGING AND INSTRUMENTATION IN RADIOLOGICAL SCIENCE

Hee-Joung Kim[1)]

1) Department of Radiological Science and Research Institute of Health Science, Yonsei University, Korea

Background

Clinical applications as well as research activities in medical imaging and instrumentation are rapidly growing fields in radiological science. Recent trends of clinical research of SPECT/CT, PET/CT, and PET/MRI as well as advanced imaging modalities indicate that clinical applications of various imaging modalities are very active, and have been triggering research activities of medical imaging and instrumentation in radiological science. Dept. of radiological science at Yonsei University is relatively new and has been focusing on both research of new technologies in medical imaging and instrumentation, and education and training of practical as well as advanced technologies in radiological science.

Methods

Recently, two international congress meetings were held and one international conference meeting will be held in 2013 in Seoul. One was the World Congress on Medical Physics and Biomedical Engineering 2006 with the theme of "Imaging the future medicine" and the other one was "9th Congress of the World Federation of Nuclear Medicine & Biology with the theme of "Global harmonization and new horizon of nuclear medicine" at the same place of Coex, Seoul, Korea. These two congress meetings may cover worldwide major research activities in medical imaging and instrumentation and played a very important role to have nationwide attention including governmental level in Korea. Recently, it's been decided to have 2013 IEEE NSS/MIC conference meeting in Seoul, Korea, and our Dept. will play a major role to host this prestigious conference meeting for the 1st time in Asia and Oceania. There are 4 Laboratories in our Dept. including medical physics and imaging Lab (MPIL), iTOMO Lab, Molecular Imaging Lab (MoIL), and magnetic resonance imaging Lab (MRIL). Major interests of iTOMO Lab includes dental panorama imaging technique, dental CT technique, dual-energy radiography imaging technique, tomosynthesis imaging algorithm, design digital processing filter and algorithm to improve image quality, and image quality estimate technique of digital radiography. MRIL has been researching on functional MRI, diffusion tensor imaging & fiber tractography, and phase contrast MR angiography. MoIL has been researching on developing both small gamma camera and small PET, and image optimization. Research interests of MPIL includes the measurements of physical characteristics of SPECT/PET/X-ray & CT, and their quantitation, imaging physics and instrumentation, and simulation of multi-modality imaging techniques. Recently, our Dept. awarded government grant of "Basic Atomic Energy Research Institute (BAERI)" which will support for next 6 years to develop functional and anatomical multi-imaging technology based on multi-energy photon counting. The purpose of this project is to develop the image acquisition technique for the optimization of multi-energy photon counting images included in functional/anatomical information and to research the functional and anatomical fused imaging on the state-of the art technologies.

Results

With these activities, in recent years, medical imaging and instrumentation, such as digital x-ray radiography, computed tomography, nuclear magnetic resonance, emission tomography, animal imaging devices, multi-modality systems, and modeling and evaluation of imaging systems, have been rapidly advancing in Korea. The Korean government has been trying to lay a foundation for medical devices and information by providing policies and systematic funding supports on the product and technology development. Based on the government's supports, there are strenuous and growing efforts to improve the nation's international competence made in research and development of medical imaging technology and its applications by universities, industries, and national science research institutes, although major research activities have been

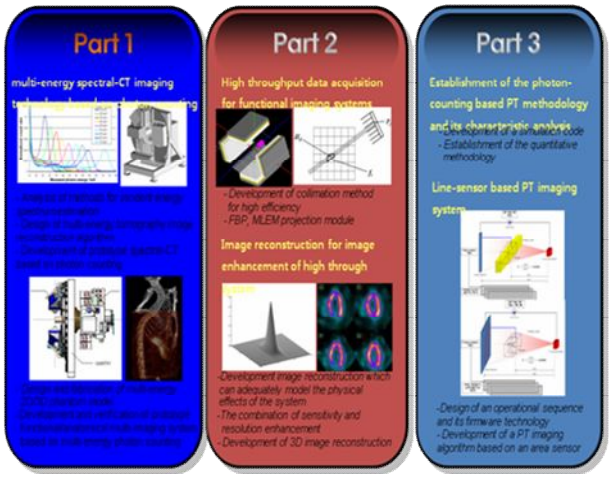

leading by academic side compared to industry side. The figure1 shows the scope of the BAERI project to be developed.

Figure 1. The scope of the development of multi-imaging technology based on photon counting

Conclusion

Summaries of the current achievements and the future prospects in the realm of medical imaging and instrumentation in our Dept. will be presented with overview of clinical applications in advanced imaging technologies. Summaries of educational system in radiological science as well as medical physics in our Dept. will also be presented.

Memo

NONINVASIVE ESTIMATION OF REGIONAL CEREBRAL BLOOD FLOW USING ^{123}I-IMP ACQUISITION DATA

Shinji Abe[1) 2)], Katsuhiko Kato[3)], Yoshitake Takahashi[4)], Masato Yamashita[2)], Naotoshi Fujita[2)], Naotoshi Ohta[5)], Yasukazu Kajita[6)], Shinji Naganawa[5)].

1) Department of Radiological Sciences, Nagoya University Graduate School of Medicine, Nagoya, Japan
2) Department of Radiological Technology, Nagoya University Hospital, Nagoya, Japan
3) Department of Radiological Technology, Nagoya University School of Health Sciences, Nagoya, Japan
4) Department of Medical Engineering, Division of Allied Health Sciences,Osaka University Medical School, Osaka, Japan
5) Department of Radiology, Nagoya University Graduate School of Medicine, Nagoya, Japan
6) Department of Neurosurgery, Nagoya University Graduate School of Medicine, Nagoya, Japan

Introduction

N-isopropyl-p [I-123] iodoamphetamin (^{123}I-IMP) is widely used as a tracer for the measurement of regional cerebral blood flow (rCBF) by single-photon emission computed tomography (SPECT). ^{123}I-IMP is one of the most suitable available SPECT tracers because the radiopharmaceuticals excel in the contrast between the cerebral normal and defective parts. Measurement of rCBF is necessary for evaluation of the cerebral circulation to understand abnormalities of blood flow and the target changes due to disease processes. In the quantification, ^{123}I-IMP has a higher first-pass extraction fraction and negligible back diffusion from cerebral tissue immediately after injection. Therefore, it is not easily influenced by metabolic activity of the tissues and indicates the good linearity of the radioactivity distribution in rCBF.

In general, arterial blood sampling and an integral of input function are needed to calculate rCBF. SPECT and continuous arterial blood sampling on the basis of the microsphere model described by Kurl et al. were used to measure rCBF with ^{123}I-IMP (1-2). Moreover, several studies have been made using a two-compartment model analysis which correlates with back diffusion of ^{123}I-IMP (3). These methods require arterial blood sampling which is invasive for patients and demanding in a daily clinical setting.

To date, there have been some reports on the estimation of rCBF by observing pharmacokinetics of ^{123}I-IMP without arterial blood sampling (4-5). However, the rCBF values estimated in these studies have not been compared with those obtained by other methods. ^{15}O-water seems to be more suitable for rCBF quantification than ^{123}I-IMP because it is not metabolized inside of the body and the extraction fraction is comparatively high (0.85-0.95) (6).

The purpose of this study was to evaluate a new noninvasive method using ^{123}I-IMP for estimation of rCBF without any blood sampling and to compare the new method with the conventional method using ^{15}O-water PET.

Materials and Methods

Consecutive 8 patients with suspected CBF disorders (age: 58±19y, male/female:4/4) underwent PET and SPECT examinations on the same day. Procedures for data acquisition by PET and gamma camera are summarized in Fig.1.

The study was performed according to the approval of the Ethics Committee of Medicine at Nagoya University for Human Studies, and informed consent was obtained from all patients before the study.

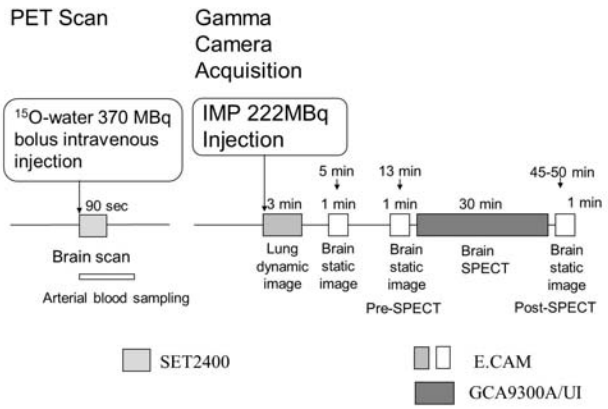

Fig.1 Outlines of the procedure of ^{15}O-water PET and ^{123}I-IMP data acquisition with gamma camera.

CBF measurement by PET was performed using ^{15}O bolus administration autoradiography method by Kanno et al. (6). PET scanner SET2400 (Shimadzu Corporation, Kyoto, Japan) and two gamma cameras E.CAM for two-detector type and GCA9300A/UI for three-detector type (Toshiba Medical systems company respectively, Nasu, Japan) were used. First, CBF measurement by PET was performed. Next, dynamic lung and static head images were acquired after injection of ^{123}I-IMP, followed by brain SPECT. Lung washout counts and the time course of brain counts were used for explanatory variables, and rCBF measured by ^{15}O-water PET is used for the dependent variables. The regression equation was calculated with both variables. The rCBF was estimated using the regression equation.

The PET and SPECT images were matched to a standard cerebral template by analytical three dimensions ROI software (7), and the accumulation ratios were calculated on each region of the brain.

Results

Examples of lung and brain images and lung washout curve for a study patient are shown in Fig. 2. Fig. 3 shows comparison of the rCBF values estimated by ^{123}I-IMP SPECT and those actually measured by ^{15}O-water PET autoradiography. A significant correlation ($r=0.93$, $p<0.001$) was detected between rCBF values measured by ^{15}O-water PET and those estimated with ^{123}I-IMP.

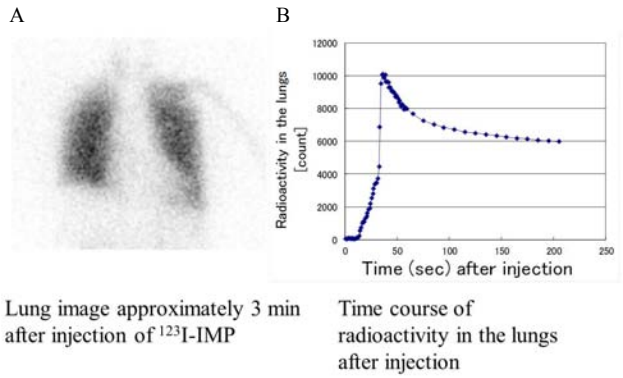

Fig.2 Data acquired after intravenous injection of ^{123}I-IMP.
(A) Lung planar image approximately 3 min after injection.
(B) Time course of radioactivity of the lungs after injection.
(C) Brain static images at 5 min, 13 min (pre-SPECT) and 45-50 min (post-SPECT) after injection.

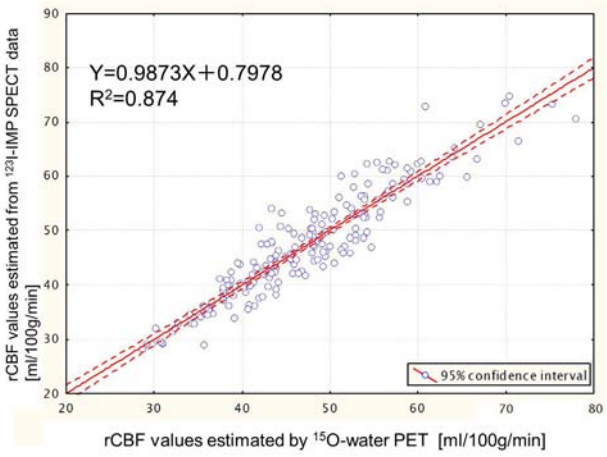

Fig.3 Comparison of the rCBF values estimated by ^{123}I-IMP SPECT and those measured by ^{15}O-water PET. There is a significant correlation between the regional CBF values obtained by these two methods (r=0.94: p<0.001).

Discussion

We demonstrated that rCBF can be estimated by using the ^{123}I-IMP initial circulation images of the lungs and brain without any blood sampling, and that the rCBF values obtained by this method showed accuracy similar to those actually measured by ^{15}O-water PET.

Furthermore, the new method proposed in this study is more useful for daily clinical rCBF quantification than the conventional methods which require arterial blood sampling.

Conclusion

The noninvasive method proposed in this study can reliably estimate rCBF using brain ^{123}I-IMP SPECT data without any blood sampling.

References

[1]Kuhl DE, Barrio JR, Huang SC, et al. Quantifying local cerebral blood flow by N-isopropyl-p [I-123] iodoamphetamin (IMP) tomography. *J Nucl Med* 1982; 23:196-203.

[2]Matsuda H, Seki H, Sumiya H, et al. Quantitative local cerebral blood flow by N-isopropyl- (iodine 123) p-iodoamphetamine and single photon emission computed tomography with rotating gamma camera. *Am J physiol Imaging* 1986; 1: 186-194.

[3]Iida H, Itoh H, Uemura K, et al. Quantitative mapping of regional cerebral blood flow using iodine-123-IMP and SPECT. *J Nucl Med* 1994; 35:2019-2030.

[4]Yonekura Y, Sugihara H, Taniguchi Y, et al. Quantification of brain perfusion SPECT with N-isopropyl-p-iodoamphetamin using noninvasive microsphere method: estimation of arterial input by dynamic imaging. *Jpn J Nucl Med* 1997; 34:901-908.

[5]Okamoto K, Ushijima Y, Okuyama C, et al. Measurement of cerebral blood flow using graph plot analysis and I-123 iodoamphetamine. *C Nucl Med* 2002; 27:191-196.

[6]Kanno I, Iida H, Miura S, et al. A system for cerebral blood flow measurement using an $H_2{}^{15}O$ autoradiographic method and positron emission tomography. *J Cereb Blood Flow Metab* 1987; 7:143-153.

[7]Takeuchi R, Yonekura Y, Matsuda H, et al. Usefulness of a three-dimentional stereotaxic ROI template on anatomically standardised ^{99m}Tc-ECD SPET. *Eur J Nucl Mol Imaging* 2002; 29:331-341

Author address

Shinji Abe
65 Tsurumai-Cho, Showa-Ku, Nagoya, 466-8560, Japan
Tel: +81-52-744-2553
abeshin-ngy@umin.ac.jp

AN INFLUENCE OF THE BEAM QUALITY ON THE NOISE OF THE IMAGE IN DIGITAL MAMMOGRAPHY

Maki Yamada[1)], Yuri Kato[1)] Naotoshi Fujita[2)], Yoshie Kodera[3)]

1) Department of Radiological Sciences, Nagoya University Graduate School of Medicine, Nagoya, Japan
2)Department of Radiological Technology, Nagoya University Hospital, Nagoya, Japan
3) Department of Radiological Technology, Nagoya University School of Health Sciences, Nagoya, Japan

Introduction

The uses of digital mammography systems have become widespread recently. However, the optimal exposure parameters are uncertain in clinical. We need to optimize the exposure parameter in digital mammography with maximization of the image quality and minimization of patient dose. The purpose of this study is to investigate an influence of the x-ray energy on the noise of the image. We obtained images for various tube voltage and the thickness of compressed breast. The noise properties of these images were evaluated with these indices: Wiener spectrum (WS), the noise equivalent number of quanta (NEQ), and signal-to-noise ratios derived from the perceived statistical decision theory model with the internal noise of eye-brain system (SNR*i*). We measure them under the fixed average glandular dose (ADG).

Materials and Methods

Equipment used in this study ; The mammography equipment used in this study was Mermaid model MGU-100B. The computed radiography (CR) reader used was REGIUS V stage, Model 190. The CR plate used was CP1M200 (with the columnar crystal phosphors). These equipments were manufactured by Konica Minolta MG. The x-ray images of low contrast objects were obtained for the measurement of the SNR*i*. To measure the contrasts and to calculate Wiener spectrum, we obtained images of acrylic steps (thickness: 1-10 mm) and uniformly exposed x-ray images. We used acrylic plates (thickness: 2, 4, 5 and 7 cm) as breast phantoms. Mo/Mo and Mo/Rh were chosen for the target/filter combinations. As the source of low contrast signal, we used a resinous disc (diameter: 4.2mm, thickness: 4.5mm). To measure the presampled modulation transfer function (MTF) for NEQ, we obtained images of the tungstenium edge.

Measurement of the average glandular dose ; We measured the average glandular dose (AGD) and chose the exposure level which gave the European Reference Organization for Quality Assured Breast Screening (EUREF) dose acceptable level for every combination of the thicknesses of phantoms and the tube voltages (25, 28, 30, 32, 35 kV). Actually, we could not adjust the exposure level for the AGD strictly because of the restriction of the machine. Therefore we selected the exposure level for EUREF dose acceptable level as near as possible (Table.1 and Table.2).

Measurement of image contrasts ; WS depends on the image contrast, and the image contrast changes with the tube voltage. For this reason, we evaluated WS under fixed image contrast. In order to do this, the image contrast of each tube voltage was measured. We obtained the images of the acrylic plates and the acrylic steps, which were put on the chest wall side of the table for the contrast evaluation (Fig. 1). We read out the raw data of the acrylic step images and found the contrast by the pixel value of each step.

Table 1. EUREF dose acceptable level for each thickness of PMMA and its equivalent breast thickness

PMMA thickness [cm]	Equivalent breast thickness [cm]	Dose acceptable level [mGy]
2	2.1	0.6
4	4.5	1.6
5	6.0	2.4
7	9.0	5.1

Table 2. Exposure level for 4-cm-thick PMMA with Mo/Mo

AGD [mGy]	25 kV	28 kV	30 kV	32 kV
	Exposure level [mAs]			
1.3	80	50	40	32
1.7	100	63	50	40

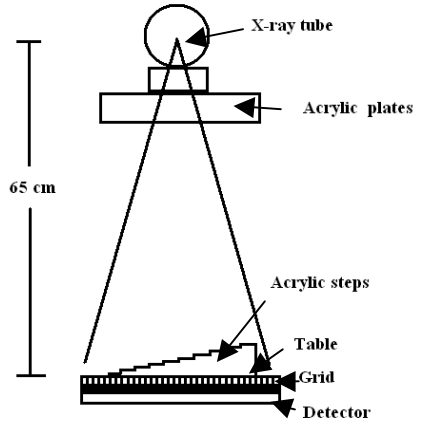

(a) Overview

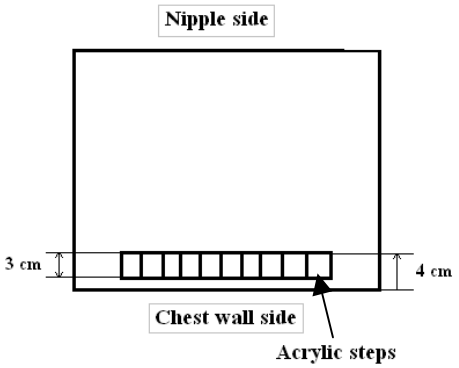

(b) Overhead view

Fig. 1 Layout of measurement of the contrast

Calculation of WS ; We calculated the WS by the two-dimensional fast Fourier transform method. When we evaluated the WS values at 25, 30, 32 and 35 kV, we adjusted the contrasts under these tube voltages to that under 28 kV. To tune the image contrasts, we computed the WS and multiplied the following correction factor *k*.

k =(image contrast at 28 kV/image contrast at an other tube voltage)^2

Calculation of NEQ ; The NEQ is described as shown below:

$$NEQ=\{(G\cdot\log_{10}e)^2MTF^2\}/\{WS_{\Delta PV}\}$$

In these figure, G means the gradient of the characteristic curve for the detector.

Calculation of SNRi ; The SNR*i*, which takes the spatial frequency response of the human visual system and the internal noise of eye-brain system into consideration, is written as

$$SNRi=SNRp/\{1+(Ni/Np)^2\}^{1/2}$$

In this formula, the SNR*p* represents the ratio of signal (S*p*) to noise (N*p*). The value of the S*p* and the N*p* were calculated in consideration of the visual spatial frequency response of the human observer [3]. The N*i* means the internal noise [4] which is inherent in an observer, for instance, the noise in relation to the neurophysiological unstableness and to fluctuations of the observer's memory.

Results

WS ; The WS was almost stable when the tube voltage changed between 2-cm and 4-cm-thick phantoms. There were few differences in the WS values for each tube voltage with 5-cm-thick phantom, and we observed the tendency that high tube voltage improves the noise property of the image. This trend was more remarkable for 7-cm-thick phantom. As the combination of target/filter, Mo/Rh was more beneficial than Mo/Mo for phantoms thicker than 4 cm. This trend was also more conspicuous for thicker phantom.

NEQ ; For 2-cm-thick phantoms, the NEQ did not change with the tube voltage and filtration except for 32 and 35 kV with Rh filter. The NEQ values on these two exposure conditions were lower than that on others. Also, 35 kV with Rh filter gave the highest NEQ for phantom thicker than 4 cm. In these cases, the superiority of Rh filter to Mo filter became clearer for thicker phantom.

SNRi ; The SNRi is shown in Figure 2. For 2-cm and 4-cm-thick objects, we recognized the tendency that the SNRi value with Mo filter was larger than that with Rh filter. The SNR*i* increased when the tube voltage decreased.

Discussion

The results of WS and NEQ indicate that when the image contrast and AGD was constant, for a phantom thinner than 5 cm, an increase of the tube voltage did not improve the noise property of images very much. The results also showed that image property with the target/filter Mo/Rh was better than that with Mo/Mo for the phantom thicker than 4 cm. In general, it is said that high tube voltage delivers fine noise property. The result of our study contradicted this common theory on the x-ray energy level for mammography.

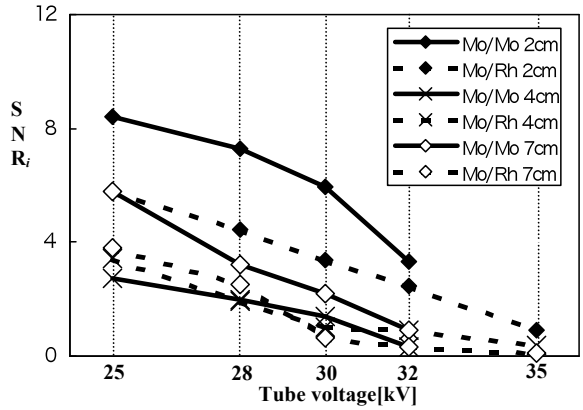

Fig.2 The results of SNRi for each thickness of phantoms

The result of SNRi differers from the results of WS and NEQ. In this study, the SNR*i* depends on the contrast of signal. We should make accuracy high with the low contrast object that has another intensity.

Conclusions

In conclusion, when the image contrast and AGD was constant, for the phantom thinner than 5 cm, an increase of the tube voltage did not improve the noise property of images very much. The results also showed that image property with the target/filter Mo/Rh was superior to that with Mo/Mo for the phantom thicker than 4 cm. Our result signified that high tube voltages did not improve the noise property of images with the x-ray energy level for mammography.

The result of SNRi conflicted with the results of WS and NEQ. We need to examine SNRi with the low contrast signal which have various intensity.

References

[1]Leh-Nien D Loo, Kunio Doi, Charles E Metz. A comparison of physical image quality indices and observer performance in the radiographic detection of nylon beads. Phys. Med. Biol., 1984;29, No. 7;837-856

[2]Masamitsu Ishida, Kunio Doi, Leh-Nien Loo, et al. Digital Image Processing: Effect on Detectability of Simulated Low Contrast Radiographic Patterns. Radiology 1984; 150: 569-575

[3]Anil K. Jain. Fundamentals of Digital Image Processing. Prentice Hall. 1989

[4]Ken Ohara, Heang-Ping Chan, Kunio Doi, et al.Investigation of basic imaging properties in digital radiography. 8. Detection of simulated low-contrast objects in subtraction angiographic images. Med. Phys 1986; 13(3): 304-311

Author address

E-Mail:yamada.maki@h.mbox.nagoya-u.ac.jp

MULTI-MATERIAL DECOMPOSITION IMAGING IN THE PHOTON COUNTING DETECTOR

Hyo-Min Cho[1)], Yu-Na Choi[1)], Hee-Joung Kim[1)]

1) Department of Radiological Science and Research Institute of Health Science, Yonsei University, Korea

Introduction

The photon counting detectors such as cadmium zinc telluride (CZT) and cadmium telluride (CdTe) have powerful advantages compared to energy integrating detectors. CZT or CdTe can detect individual gamma-ray or x-ray photon with energy discrimination. In recent years, energy-resolving and material decomposition x-ray imaging based on photon counting detectors has attracted attention from biomedical imaging researchers. One group has reported two contrast agents could be distinguished by the k-edge CT image using photon counting detectors.

Monte Carlo simulation is an essential tool in emission and transmission imaging that can assist in the design of new medical imaging devices, the optimization of acquisition protocols and the development or assessment of image reconstruction algorithms and correction techniques. This year, the OpenGATE collaboration has released GATE 6.0, supporting simulations of radiotherapy and computed tomography. They provide geometry of computed tomography with photon counting based readout.

We evaluated a large-area CZT detector originally built as a radionuclide detector for a small animal SPECT/CT system in combination of a microfocus x-ray source with a general goal of developing a material-decomposition imaging method. In addition, the characteristic study of two photon counting materials, CZT and CdTe were evaluated in the GATE environment.

Materials and Methods

The presentation will describe the basic principles of multi-material decomposition imaging based on photon counting detector. The experimental results from a feasibility study of multi-material decomposition imaging using the developed small animal SPECT/CT system will be presented. In addition, the simulation results for the characteristic of photon counting detector and multi-energy imaging of multi-material phantom will be presented.

Experimental feasibility of multi-material decomposition imaging

The characteristics of x-ray tube from Oxford Instruments (Scotts Valley, CA, USA) are; tungsten anode, source size 80 μm x 70 μm, maximum operating current 1 mA, and maximum accelerating voltage 60 kV. The 2 mm thick aluminum filter was used to attenuate x-rays with energies below the noise floor of the detector.

The large area photon counting CZT detector manufactured by Gamma Medica Ideas (Northridge, CA, USA) was used. The detector has an active detection area of 20 x 20 cm2, with multiple modules tiled together. The detector is configured as a 5 x 5 array of CZT modules, each with a 16 x 16 array of pixels and a pixel width of 2.5 mm. Thus, the used CZT detector is an 80 x 80 pixel array covering an active area of 20 x 20 cm2 with a crystal thickness of 2.5 mm.

For the feasibility study of multi-material decomposition imaging a phantom that included various materials was built. We designed the phantom using a 15 x 15 cm2 piece of cellophane. We had attached 7 materials, with a range of densities and atomic numbers, on the cellophane. The materials are including glass (silicon dioxide), highly ordered pyrolytic graphite (HOPG), clay, titanium, plastic, aluminum, buffalo nickels, walking liberty half dollar coin.

The CZT detector was positioned 84.3 cm from the x-ray tube focal spot. The phantom was taped in contact with, and centered on, the CZT detector. The multi-material x-ray images were obtained at 50 kVp, 0.5 mA, and images were acquired for 140 sec/image. Acquired images corrected for bad pixels, gain, and offset. The attenuation of each material was obtained by the ratio of the emergent and incident radiation intensities I/I0 according to the x-ray energy.

CZT detector in x-ray spectroscopy with different pixel sizes and pitches

GATE version 6.0 was used to perform an accurate simulation of the different pixel sizes. In this simulation study, charge sharing and pulse pileup were not considered. The Cd1-xZnxTe detector (x = 0.1, density = 5.68 g/cm3) used in this study. The CZT detector was 10x10 mm2 and thickness of 3 mm. The thickness was chosen since it allows >90% absorption of the photons at 120 kVp. In an attempt to evaluate the detection ability, we designed the CZT detector with different pixel size on GATE. The pixels with sizes of 0.09 ×0.09, 0.45 ×0.45, and 0.90×0.90 mm2 were simulated.

Energy resolved photon counting x-ray imaging with CZT detector

We designed a cylindrical PMMA phantom including three Iodines in concentration of 140, 40, and 8 mg/cm3 and one Gadolinium in concentration of 39.3 mg/cm3. We studied the ability to separate different materials from the multi-energy windows. We obtained images from 23-32, 33-42, 40-49 and 50-59 keV energy windows. For each energy windows the contrast-to-noise ratio (CNR) was considered to be the image quality.

Results

Measured attenuation of each material was in a good agreement with the reference data of the NIST physics laboratory. The attenuation of x-rays in the various materials is dependent on the energy of the x-rays and the atomic composition of the material.

Three different pixel spectrums were distorted towards the lower energy region. Because the characteristic x-rays add counts in the range of 20-40 keV. The photoelectric effect is dominant at Cd and Te of CZT material due to the high Z numbers. The Z numbers of Cd and Te are 48 and 52. As characteristic x-rays of Cd and Te process quite high energy, they escape from crystals. Especially, these effects are evident in the small pixel sizes.

For Iodine, the CNR was found to dramatic increase in the range of 33-42 keV. For Gadolinium, the calculated value of

the CNR in the range of 50-59 keV was higher than those below 50 keV. Because the photons with energy levels just above the K-edge energy are more likely to be absorbed than photons with energy levels just below the K-edge energy.

Conclusions

We demonstrated that multi-material decomposition imaging is experimentally feasible using the photon-counting CZT detector and polychromatic x-ray. The photon counting based functional and anatomical imaging system will be designed in the GATE.

DOSIMETRIC CHARACTERIZATON OF FLATTENING FILTER FREE LINAC USING MONTE CARLO SIMULATION

Takuma Matsunaga[1)], Tomohiro Shimozato[2)], Yuichi Aoyama[3)], Hiroshi Fukuma[4)], Ryuichi Yada[5)], Hiraku Fuse[1)], Yusuke Oribe[1)], Masataka Komori[2)], Yasunori Obata[2)]

1) Department of Radiological Sciences, Nagoya University Graduate School of Medicine, Nagoya, Japan
2) Department of Radiological Technology, Nagoya University School of Health Sciences, Nagoya, Japan
3) Department of Radiology, Nagoya University Hospital, Nagoya, Japan
4) Central Department of Radiology, Nagoya City University Hospital, Nagoya, Japan
5) Department of Radiology, Seirei Hamamatsu General Hospital, Hamamatsu, Japan

Introduction

The flattening filter (FF) of medical linac is placed in the photon beamline to produce a flat beam profile at the given depth, but it decreases primary beam intensity by scattering and absorption. Recently some researches have shown that removing FF from medical linac can increase dose rate considerably, and reduce out-of-field doses [1-4]. In this study, we provide dosimetric properties of 6 MV and 10 MV photon beams from FF free (FFF) linac using Monte Carlo (MC) simulation.

Materials and Methods

MC modeling of medical linac with and without FF: We have developed 6 MV and 10 MV photon beam model for the linac head of Varian Clinac series accelerator using EGSnrc/BEAMnrc MC code [5]. The linac head components, including target, primary collimator, vacuum window, FF, monitor ion chamber, mirror, and X and Y jaws, were simulated on the basis of manufacturer-provided information. To calculate dose distributions in water phantom, we applied EGSnrc/DOSXYZnrc MC code [6].

The initial electron beam incident on the target have the distribution of the electron energy and the radial intensity assumed Gaussian in shape[7], and mean energy and intensity distribution of the initial electron is not clearly and varies among the same model of linacs. To determine electron energy, we comparing the measured and calculated percentage depth dose (PDD) for 30 x 30 cm^2 field size. After initial electron energy selection, we determined intensity distribution comparing the measured and calculated off-center ratio (OCR) at the depth of 10 cm for 5 x 5, 10 x 10, 20 x 20, and 30 x 30 cm^2 field sizes. To compare the measured and calculated dose, local dose difference were calculated by following equation:

$$Local\ dose\ difference = \left[\frac{dose_{measurement} - dose_{MC}}{dose_{measurement}}\right]$$

The mean energy of the initial electron and the distributions of the electron energy and the radial intensity are shown in Table 1. Using determined initial electron, the phase-space (PS) file, containing data relating to particle position, direction, charge, and energy for 5 x 5, 10 x 10, 20 x 20, and 30 x 30 cm^2 field sizes at source surface distance (SSD) of 100 cm with and without FF were produced.

Table 1 Initial electron parameters. The energy and intensity spread is given at FWHM

Nominal energy (MV)	Derived energy (MeV)	Energy spread FWHM	Intensity spread FWHM (cm)
6	6.0	3%	0.15
10	10.5	3%	0.15

Dosimetric properties of FFF linac: To find out the characteristic of FFF linac, we compared PDD and OCR for varied field sizes, dose per incident electron, planer fluence, energy fluence, and energy spectrum with standard linac using EGSnrc/DOSXYZnrc and BEAMDP sub code [8].

Results and Discussion

Validation of MC modeling: To validate our MC simulation, calculated PDD and OCR were compared with measurement data. There were good agreement between MC and measurement results, and local differences were less than 3% in all region. The examples of calculated and measured PDD and OCR are shown in Fig. 1 and 2, respectively.

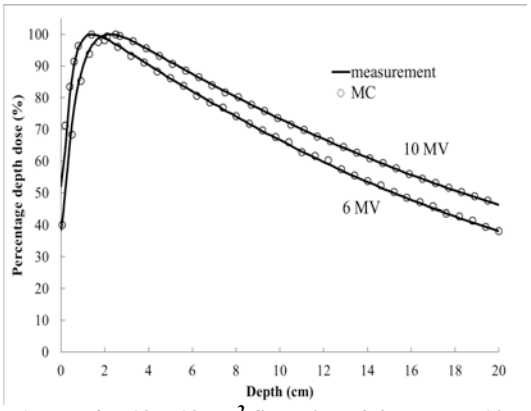

Fig. 1 PDD for 10 x 10 cm^2 field size of 6 MV and 10 MV. Monte Carlo is circle and measurement is solid.

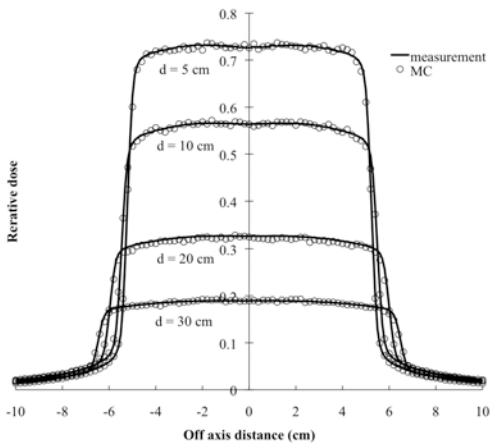

Fig. 2 OCR at the depth of 5 cm, 10 cm, 20 cm, and 30 cm for 10 x 10 cm^2 field size of 6 MV. Monte Carlo is circle and measurement is solid.

Dosimetric properties of FFF linac: We considered dose per initial electron at the depth of 10 cm for dose rate comparison. For 10 x 10 cm^2 field size, the ratios of dose per initial electron for FFF linac to standard linac were 2.38, 5.17 for 6 MV, 10 MV, respectively.

The depth dose and OCR were calculated for field sizes of 5 x 5, 10 x 10, 20 x 20, and 30 x 30 cm^2. The depth dose curves of FFF linac for 10 x 10 cm^2 field for 6 MV and 10 MV, are shown in Fig. 3 and 4, respectively. The depth dose was normalized at maximum point of measurement with FF. In the beyond maximum dose region, the dose for standard linac is higher than that for FFF linac due to the beam hardening effect of the FF. In the build up region, because of softer spectra and contamination low-energy electron, FFF linac delivers higher dose than standard linac. Especially, for 10 MV, significant increasing dose in the build up region is observed due to the excessive contamination electron. It seems that more penetrating electron through the target reach the phantom for 10 MV than for 6 MV, because the target of 6 MV is tungsten and copper, but that of 10 MV is copper only.

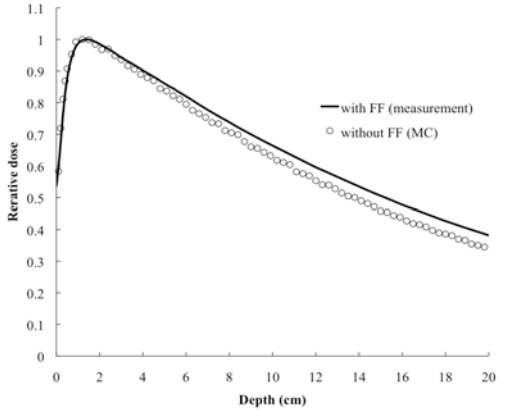

Fig. 3 Comparison of depth dose for with and without FF for 10 x 10 cm^2 field size of 6 MV. without FF, MC is circle and with FF, measurement is solid.

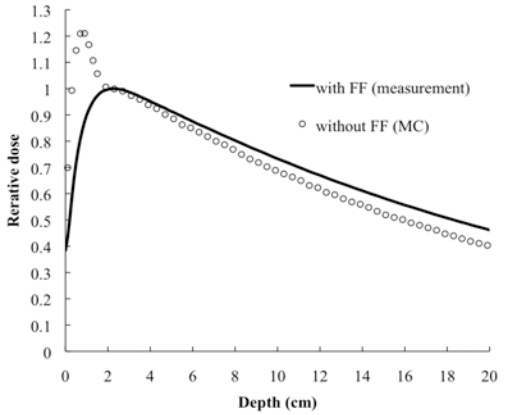

Fig. 4 Comparison of depth dose for with and without FF for 10 x 10 cm^2 field size of 10 MV. without FF, MC is circle and with FF, measurement is solid.

The OCR at the depth of 10 cm of 10MV FFF linac for 10 x 10 cm^2 is shown in Fig. 5. OCR was normalized at the central axis dose. By removing of FF, the dose was reduced with distance from the central axis. In addition, removed FF reduced the out-of-field dose. For example, in Fig. 5, at a distance of 7 cm from the central axis, the ratio of doses for FFF linac to standard linac was 0.8. This is because photon fluence was reduced with distance from central axis as a result that removing FF reduced scattering radiation from linac head.

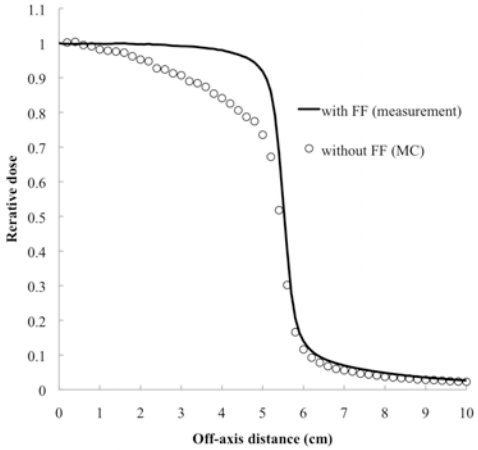

Fig. 5 Comparison of OCR at the depth of 10 cm for with and without FF for 10 x 10 cm^2 field size of 10 MV. without FF, MC is circle and with FF, measurement is solid.

Conclusions

The MC model of Varian Clinac series accelerator with and without FF were developed and compared. Our results shows that removing FF can increase dose rate and decrease out-of-field dose. These could be an advantage of FFF linac, but for clinical usage, FFF linac should equip the filter to remove the excessive contamination electron.

References

[1]Oleg N Vassiliev, Uwe Titt, Falk Pönisch, Stephen F Kry, Radhe Mohan, Michael T Gillin. Dosimetric properties of photon beams from a flattening filter free clinical accelerator. *Phys. Med. Biol.* 2006;51:1907-1917.

[2]Oleg N Vassiliev, Uwe Titt, Stephen F Kry, Falk Pönisch, Michael T Gillin, Radhe Mohan. Monte Carlo study of photon fields from a flattening filter-free clinical accelerator. *Med. Phys.* 2006;33:820-827.

[3]Asghar Mesbahi. Dosimetric characteristics of unflattened 6 MV photon beams of a clinical linear accelerator. *Appl. Radiat. Isot.* 2007;65:1029-1036.

[4]Gabriele Kragl, Sacha af Wetterstedt, Barbara Knäusl, Mårten Lind, Patrick McCavana, Tommy Knöös, Brendan McClean, Dietmar Georg. Dosimetric characteristics of 6 and 10 MV unflattened photon beams. *Radiother Oncol.* 2009;93:141-146.

[5]D.W.O. Rogers, B. Walters, I. Kawrakow. BEAMnrc Users Manual. *NRCC Report PIRS-509 (A) revK.* 2009.

[6]B. Walters, I. Kawrakow, D.W.O. Rogers. DOSXYZnrc Users Manual. *NRCC Report PIRS-794 revB,* 2009.

[7]Daryoush Sheikh-Bagheri, D. W. O. Rogers. Sensitivity of megavoltage photon beam Monte Carlo simulations to electron beam and other parameters. *Med. Phys.* 2002;29:379-390.

[8]C.-M. Ma, D.W.O. Rogers. BEAMDP Users Manual. *NRCC Report PIRS-0509 (C) revA.* 2009.

Author address

E-Mail: matsunaga.takuma@h.mbox.nagoya-u.ac.jp

ESTIMATION OF RADIATION DOSES FROM X-RAY CT USING MONTE CARLO SIMULATION

Yuki Morishita [1)], Shuji Koyama [1)]

1) Department of Radiological Sciences, Nagoya University Graduate School of Medicine, Nagoya, Japan
2) Department of Radiological Technology, Nagoya University School of Health Sciences, Nagoya, Japan

Introduction

The purpose of this study is to calculate accurate radiation dose in patient from CT examination using voxel phantom. In the calculation, scanner-specific descriptions that include filtration designs, an orbital overlap and the absorption of CT table are necessary. A special filter called "beam-shaping filter" which is positioned in front of the x-ray tube of the CT units causes less uniform x-ray fan beam(Figure 1). We took into account the effect of the filter based on measured data in this simulation.

A standard Japanese Model can be developed by using the voxel phantom from CT DICOM(Digital Imaging and Communication in Medicine) format data. In-phantom dosimetry system, as will hereinafter be described in detail, was used to compare the measurements and the calculations.

Materials and Methods

1. Overview

All simulations were performed using the EGS5 (Electron Gamma Shower ver.5) Monte Carlo code, which is a general purpose package for the Monte Carlo simulation of the coupled transport of electrons and photons in an arbitrary geometry for particles with energies above a few keV up to several hundred GeV. For measurements and simulations, a Non-helical X-ray CT unit TCT-300 (Toshiba Medical Systems, Tochigi, JAPAN) was used in this study. The x-ray tube voltage was 120kV.

2. Effect of beam-shaping filter

A typical CT scanner is equipped with x-ray beam filtration that includes the beam-shaping filter. This filtration modifies a number of x-ray beam properties (effective energy, flux, first and second order statistics), making them non-uniform across the fan beam. The beam-shaping filter is used to adjust the beam quality of x-rays after passing through a patient. There is no such published data on the design of beam-shaping filter, which may vary considerably from scanner to scanner. We measured aluminum Half Value Layer(AL HVL) and dose value after passing through the beam-shaping filter and incorporated measured values in the simulation. New type of semiconductor dosimeter called Rapidose(Radcal, Monrovia, CA) was used for the measurements. Rapidose has functions that can measure dose and AL HVL at the same time and it is suitable for measurement of relatively high energy x-ray such as x-ray CT. In the measurement of the effect of beam-shaping filter, x-ray tube was fixed on the 0:00 position on its orbital. Along a fan beam of x-ray CT, Rapidose was moved up to 19 degrees measured at every one degree. In the simulation, photon number at each beam angle along the fan beam was determined by dose profiles and energy spectrums were generated by Birch's formula based on AL HVL measured on each angle was used.

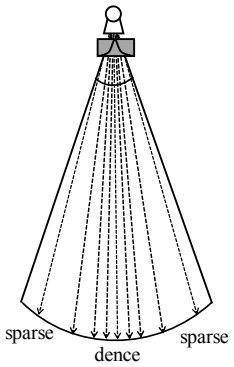

Fig.1 Incident photon number at each beam angle

3. Specific factors related to the CT device

There are several specific factors that are related to the CT scanner. Non-helical CT scanner has x-ray tube orbital overlap that cause the positions of the x-ray beam overlap on the patient. The overlap angle was adjusted to match the measured CTDI values in the simulation because the information of the actual overlap angles wasn't published by the manufacturer. A full of x-ray tube rotation was estimated at 376 degrees including overlap of -/+8 degrees.

The table top is usually made of carbon fiber due to its strength and low x-ray attenuation properties. In this simulation, the CT table was composed of density adjusted carbon. The density of the carbon was adjusted to correspond with the actual dose ratio table(+)/(-). These factors were also incorporated in the simulation code.

4. Measurement and calculation of CTDI

Computed Tomography Dose Index (CTDI) measured by using a CT acrylic phantom was used for comparison between the measurement and the calculation. The CTDI phantom is 15 cm in length with a diameter of 30 cm. CTDI values are shown in air kerma (kinetic energy released in matter ; mGy) in the phantom's center hole and four peripheral holes (0°,90°,180°,270°). In order to determine the air kerma from CT examination, simulated deposit energies in units of MeV/gram/source-particle were converted to air kerma in units of mGy by a conversion factor(C_f) [1]. An in-air normalization method that is based on pencil-chamber exposure reading for a single axial scan was taken at the isocenter of the CT gantry free in air. The conversion factor was defined as

$$C_f = \frac{(CTDI_{100,\mathrm{air,\,measured\,per\,mAs}})}{(CTDI_{100,\mathrm{air,\,simulated\,per\,particle}})} \quad (1)$$

where $CTDI_{100,\,air\,,\,measured\,per\,mAs}$ is measured by an ion chamber free in air of the x-ray CT isocenter, and $CTDI_{100,\,air\,,\,simulated\,per\text{-}particle}$ is obtained by simulation.

The absorbed dose D_{ab} is calculated by

$$D_{ab} = D_{sim} \times C_f \quad (2)$$

where D_{sim} is the calculated dose in the simulation.

5. Development of voxel phantom

Two different types of voxel phantoms were developed based on CT image. One of them(THRA-1, Kyoto Kagaku Co., Kyoto, JAPAN) is only composed of lung, bone and soft tissue but can obtain organ doses using a number of internal semiconductor dosimeter installed at the position of tissues and organs [2]. The semiconductor dosimeter is implanted in the centroid of the organ and tissue. This system is called "in-phantom dosimetry system" and was used to compare measurements and calculations. Measurements and calculations were perfomed on thoracic scan protocol. The resolution of the axial simulation matrix was decreased from 512 × 512 to 170 × 170 to decrease runtime of the simulation. The size of each voxel was $0.1875 \times 0.1875 \times 1.0$ cm^3.

Another phantom called CTU-41(Kyoto Kagaku Co., Kyoto, JAPAN) includes the shapes of organs with individual densities. The average radiation dose to each organ was estimated in CTU-41 phantom. Both "in-phantom dosimetry system" and CTU-41 phantom were scanned by x-ray CT, and image data was output as DICOM format. The organs and tissues were assigned in each voxels using digital value(Hounsfield Unit).

Results and Discussions

1. Effects of the beam-shaping filter

Figure 2 shows the dose distributions and energy changes along the beam angle. The effective energy of x-ray beam determined using the measured AL HVL. Relative dose value maintained the same level from 0 degree to ±4 degree, and after that it rapidly decreased as the angle became bigger. Similarly, effective energy maintained up to ±4 degree, and then it rapidly increased as the angle became bigger and was saturated up from ±9 degrees. The cause of the effect was that the thickness of the filter was bigger as the beam angle was bigger.

2. Comparison of CTDI between measurements and calculations

Table 1 shows comparison of measurements and calculations of the CTDI. The agreement between measurements and calculations was within 2.8 %. The CTDI at 0° position was highest due to x-ray tube orbital overlap and lowest at 180° position due to absorption of the CT table. The simulated CTDI values were approximately equal to measured CTDI values. With this result, the x-ray source and the geometry of x-ray CT could be incorporated in the simulation successfully.

3. The result of calculation using voxel phantom

The result of the comparison of measurement and calculation of the in-phantom dosimetry system is shown in Figure 3(a). Locations of the calculation point were accorded with that of semiconductor dosimeters in the phantom. Measurement and calculation shown the same tendency on the same location in the phantom, but calculated values were generally slightly greater than measured values.

Figure 3(b) shows comparison of the organ doses between in-phantom dosimetry system and CTU-41 phantom. Dose values of in-phantom dosimetry system were measured value, those of CTU-41 phantom were converted from deposited energy for each of whole organ by simulation. Calculated dose of the organ in the scan area such as lung was approximately equal to measurement dose, but the organ dose of proximity to the end of scan area such as thyroid resulted in significantly different from measured dose. In the calculation, the deposited energy in whole organ was divided by the organ mass and this value was presented as an average organ dose. When the organ was partially irradiated in the end of the scan area, average organ dose was smaller than the whole-organ irradiated case. In the measurement, the organ dose was presented maximum value as is the case in whole-organ irradiation if the evaluated point as a centroid of the organ fell within the scan area.

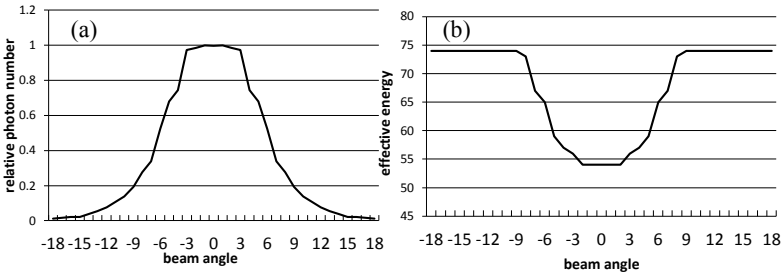

Fig.2 Relative dose and effective energy measured by Rapidose at each beam angle. (a)The relative dose at each beam angle. (b)The effective energy calculated by measured Half Value Layer at each beam angle.

Table 1 Comparison of measurements and calculations of the CTDI.

position of the dosimeter	measurement [mGy]	simulation [mGy]	difference [%]
top	21.0	20.8	-1.2
center	11.7	11.5	-1.4
left	16.6	16.5	-0.4
right	16.0	16.5	2.8
bottom	14.8	14.5	-2.4

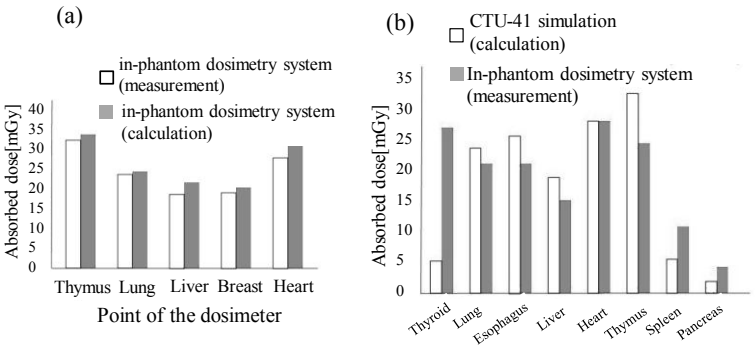

Fig.3 Comparison of measurement and calculation (a) point dose evaluation with same phantom (b)whole organ dose versus point dose

References

[1]J Gu et al , The development, validation and application of a multi-detector CT(MDCT) scanner model for assessing organ doses to the pregnant and the fetus using Monte Carlo simulations, Physics in medicine and biology

[2] Radiation dose evaluation in 64-slice CT examinations with adult and paediatric anthropomorphic phantoms

Author address

E-Mail: morishita.yuki@e.mbox.nagoya-u.ac.jp

EVALUATION OF THE DISTRIBUTION OF INTRACRANIAL NAVIGATION ACCURACY IN IMAGE-GUIDED NEUROSURGERY

Takashi Mitsui[1)], Masatoshi Tsuzaka[2)], Yuichiro Hayashi[3)], Yoshinori Asahina[1)], Kentaro Sugiura[1)], Masazumi Fujii[3)], Toshihiko Wakabayashi[3)]

1) Department of Radiological Sciences, Nagoya University Graduate School of Medicine, Nagoya, Japan
2) Department of Radiological Technology, Nagoya University School of Health Sciences, Nagoya, Japan
3) Department of Neurosurgery, Nagoya University Graduate School of Medicine, Nagoya, Japan

Introduction

Nagoya University Hospital has introduced a neuronavigation system for accurate resection of malignant brain tumors. Surgeons can confirm the positional relationship between tumors and normal tissue by using this system. Especially, this system is very useful in the resection of tumors located near the functional areas.

Accuracy of a neuronavigation system is very important to ensure a safe and accurate resection [1]. Various factors influence the navigation accuracy [2]; one of the important factors is the configuration of the fiducial markers that are positioned on the patient's head. A fiducial marker is the reference point of the navigation system (**Fig. 1**). The configuration of fiducial markers varies among institutions, and it can influence intracranial navigation accuracy. In this study, we investigated the effect of the configuration of fiducial markers on the distribution of intracranial navigation accuracy.

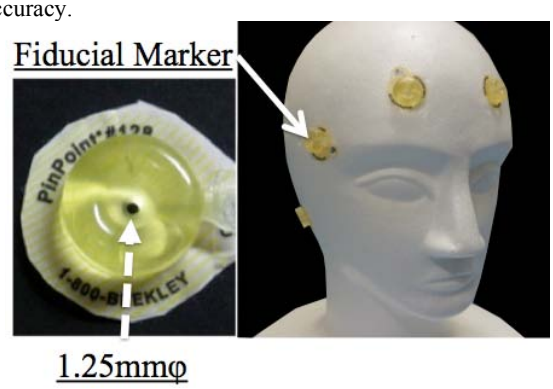

Fig. 1 Fiducial marker (doughnut shape)
A fiducial marker is used as a reference point of the navigation. They are positioned on the patient's head before surgical operation.

Materials and Methods

We evaluated intracranial navigation accuracy for 2 different configurations of fiducial markers (the clustered and scattered patterns) by using a skull-shaped phantom (**Fig. 2**). Because this phantom structurally resembles the human head, intracranial navigation accuracy can be measured in keeping with the clinical situation. We also measured the navigation accuracy by varying the number of fiducial markers. We set 4, 5, or 6 markers on the surface of the phantom for each configuration. In the clustered configuration, the markers were placed on the frontal, temporal, and occipital bones. In the scattered pattern, they were placed on the forehead, temple, and mastoid regions, same as Nagoya University Hospital's method. To measure the navigation accuracy, fiducial markers were positioned on the bottom of the phantom. And to measure the navigation accuracy on the central portion of the phantom, 5 columns and 2 circular plates were constructed inside the phantom. We can investigate the distribution of the navigation accuracy by using 27 fiducial markers positioned inside the phantom (**Fig. 3**). The phantom was filled with nickel chloride, and magnetic resonance images were acquired. MR imaging was performed with 0.4T MRI (APERTO Inspire; Hitachi Medical Co., Chiba, Japan). MR images were transferred to a planning system for navigation (iPLAN cranial; BrainLAB AG, Heimstetten, Germany), and registration points were set up on each fiducial marker positioned surface of the phantom. Registration is performed before surgery and is the process of integrating image-space coordinates with real-space coordinates. The steps of registration are as follows: (1) The operator registers the center of the fiducial markers as registration points by using the iPLAN software. (2) Registration is completed by pointing the center of each fiducial marker by using a navigation pointer. After registration was carried out using a navigation system (VectorVision Compact; BrainLAB AG), intracranial navigation accuracy was measured.

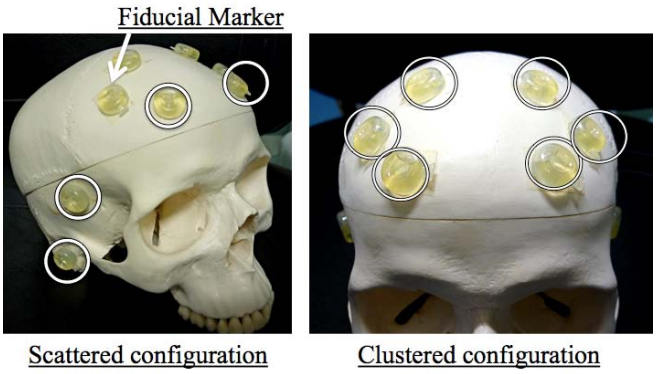

Fig. 2 Skull-shaped phantom with fiducial markers
For the scattered configuration, the fiducial markers were placed on the forehead, temple, and mastoid regions (left). For the clustered configuration, the fiducial markers were placed on the frontal, temporal, and occipital bones (right).

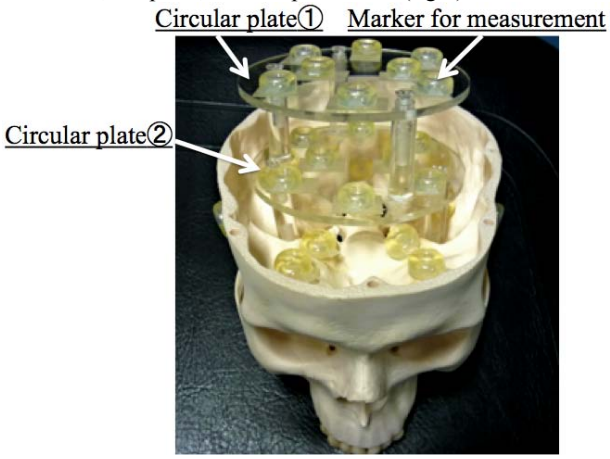

Fig. 3 Measurement point of the phantom
We can investigate the navigation accuracy by using 27 fiducial markers positioned inside the phantom. Eight fiducial markers

were positioned on each circular plate. Also, 4, 2, and 5 fiducial markers were positioned on the anterior, middle, posterior cranial fossa respectively.

Results

The mean intracranial navigation accuracy for the clustered pattern with markers placed on the frontal bone was 2.13 ± 1.15 mm with 4 markers, 1.92 ± 1.28 mm with 5 markers, and 2.01 ± 1.02 mm with 6 markers. The mean intracranial navigation accuracy for the scattered pattern was 1.51 ± 0.88 mm with 4 markers, 1.68 ± 0.75 mm with 5 markers, and 1.24 ± 0.37 mm with 6 markers (**Table 1**). The scattered patterns were significantly better than the clustered pattern ($p < 0.05$). We calculated the navigation accuracy on the central portion of the phantom and bottom of the phantom separately (**Table 2**). The accuracy for the clustered pattern with 6 markers was 1.60 ± 0.53 mm on the central portion and 2.59 ± 1.26 mm on the bottom of the phantom ($p < 0.05$). The clustered pattern could maintain the accuracy only within a narrow region near the fiducial markers positioned on the surface of the phantom. In addition, the clustered patterns with markers positioned on the temporal and occipital bones indicated a similar tendency. However, the accuracy for the scattered pattern with 6 markers was 1.17 ± 0.37 mm on the central portion and 1.37 ± 0.35 mm on the bottom of the phantom, and there was no significant difference. Thus, the scattered pattern could maintain the accuracy over a wide region of the phantom.

Table 1 Intracranial navigation accuracy

Configuration	Number	The mean (±SD) navigation accuracy (mm)
Clustered	4	2.13 ± 1.15
	5	1.92 ± 1.28
	6	2.01 ± 1.02
Scattered	4	1.51 ± 0.88
	5	1.68 ± 0.75
	6	1.24 ± 0.37

Table 2 Navigation accuracy on the central and bottom of the phantom

Configuration	Number	Central portion (±SD) (mm)	Bottom (±SD) (mm)
Clustered	4	1.72 ± 0.59	2.72 ± 1.47
	5	1.36 ± 0.59	2.73 ± 1.56
	6	1.60 ± 0.53	2.59 ± 1.26
Scattered	4	0.96 ± 0.14	2.32 ± 0.89
	5	1.39 ± 052	2.10 ± 0.83
	6	1.15 ± 0.37	1.37 ± 0.35

Discussion

The configuration of the fiducial markers varies among institutions and it influence the distribution of the navigation accuracy. It is difficult to measure intracranial navigation accuracy in clinical practice [1]. Therefore, we evaluated the effect of the configuration of the markers on the navigation accuracy by using a skull-shaped phantom. Because this phantom structurally resembles the human head, intracranial navigation accuracy can be measured in keeping with the clinical situation.

The clustered pattern, regardless of the installation location, could maintain the navigation accuracy only within the narrow region near the fiducial markers. The navigation accuracy decreased with an increase in the distance from the fiducial markers positioned on the surface of the phantom. However, the scattered pattern showed high accuracy on the entire phantom, with two exceptions: the scattered pattern with 4 and 5 markers could not maintain high accuracy on the bottom of the phantom because fiducial markers positioned on the mastoid were not used. To maintain a high accuracy on the entire phantom, it is necessary to position the fiducial markers across a wide area on the head. If a tumor exists on the base of skull or if the tumor is huge, the scattered configuration is appropriate for safe surgery.

Conclusions

In this study, we evaluated the effect of the configuration of the fiducial markers on the distribution of the navigation accuracy by using a skull-shaped phantom. It is important to position the fiducial markers across a wide area on the head for accurate resection of the tumor.

References

[1] Fitzpatrick JM, West JB, Maurer CR Jr : Predicting Error in Rigid-Body Point-Based Registration, IEEE Trans Med Imaging, 17(5), 694-702, 1998.

[2] Steinmeier R, Rachinger J, Kaus M, Ganslandt O, Huk W, Fahlbusch R. : Factors Influencing the Application Accuracy of Neuronavigation System. Stereotact Funct Neurosurg, 75:188-202, 2000.

Author address

E-Mail: mitsui.takashi@e.mbox.nagoya-u.ac.jp